Journal of Nuclear Science and Technology

ISSN: (Print) (Online) Journal homepage: https://www.tandfonline.com/loi/tnst20

Neutron total and capture cross-section measurements of ^{155}Gd and ^{157}Gd in the thermal energy region with the Li-glass detectors and NaI(Tl) spectrometer installed in J-PARC·MLF·ANNRI

Atsushi Kimura, Shoji Nakamura, Shunsuke Endo, Gerard Rovira, Osamu Iwamoto, Nobuyuki Iwamoto, Hideo Harada, Tatsuya Katabuchi, Kazushi Terada, Jun-ichi Hori, Yuji Shibahara & Toshiyuki Fujii

To cite this article: Atsushi Kimura, Shoji Nakamura, Shunsuke Endo, Gerard Rovira, Osamu Iwamoto, Nobuyuki Iwamoto, Hideo Harada, Tatsuya Katabuchi, Kazushi Terada, Jun-ichi Hori, Yuji Shibahara & Toshiyuki Fujii (2023) Neutron total and capture cross-section measurements of ^{155}Gd and ^{157}Gd in the thermal energy region with the Li-glass detectors and NaI(Tl) spectrometer installed in J-PARC·MLF·ANNRI, Journal of Nuclear Science and Technology, 60:6, 678-696, DOI: 10.1080/00223131.2022.2134224

To link to this article: https://doi.org/10.1080/00223131.2022.2134224

JOURNAL OF NUCLEAR SCIENCE AND TECHNOLOGY
2023, VOL. 60, NO. 6, 678–696
https://doi.org/10.1080/00223131.2022.2134224

ARTICLE

Neutron total and capture cross-section measurements of ^{155}Gd and ^{157}Gd in the thermal energy region with the Li-glass detectors and NaI(Tl) spectrometer installed in J-PARC·MLF·ANNRI

Atsushi Kimura[a], Shoji Nakamura[a], Shunsuke Endo[a], Gerard Rovira[a], Osamu Iwamoto[a], Nobuyuki Iwamoto[a], Hideo Harada[a], Tatsuya Katabuchi[b], Kazushi Terada[c], Jun-ichi Hori[c], Yuji Shibahara[c] and Toshiyuki Fujii[d]

[a]Nuclear Science and Engineering Center, Japan Atomic Energy Agency, Ibaraki, Japan; [b]Laboratory for Zero-Carbon Energy, Tokyo Institute of Technology, Tokyo, Japan; [c]Institute for Integrated Radiation and Nuclear Science, Kyoto University, Sennan-gun, Japan; [d]Graduate School of Engineering, Osaka University, Osaka, Japan

ABSTRACT

Neutron total and capture cross–section measurements of ^{155}Gd and ^{157}Gd were performed with Li-glass detectors and a NaI(Tl) spectrometer in the ANNRI at the MLF of the J-PARC. The neutron total cross sections were determined in the energy region from 5 to 100 meV, and those at the thermal neutron energy were obtained to be 59.4 ± 1.7 and 251.9 ± 4.6 kilobarn for ^{155}Gd and ^{157}Gd, respectively. The neutron capture cross sections were determined in the energy region from 3.5 to 100 meV with an innovative method, and those at the thermal energy were obtained as 59.0 ± 2.5 and 247.4 ± 3.9 kilobarn for ^{155}Gd and ^{157}Gd, respectively. The present total and capture cross sections agree well within the standard deviations. The results for ^{155}Gd were found to be consistent with the values in JENDL-4.0 and the experimental data given by Møller et al., Mastromarco et al. and Leinweber et al. Those for ^{157}Gd agreed with the evaluated data in JENDL-4.0 and the experimental data by Møller et al. and Mastromarco et al. However, they disagree (11% larger) with the experimental result by Leinweber et al.

ARTICLE HISTORY
Received 19 August 2021
Accepted 30 September 2022

KEYWORDS
^{155}Gd; ^{157}Gd; neutron total cross section; neutron capture cross section; J-PARC; MLF; ANNRI; neutron TOF

1. Introduction

Throughout a reactor operation, the reactivity decreases since fissile materials, such as ^{235}U, are consumed and fission product nuclides, some of which are efficient neutron absorbers, are generated. As a result, a positive (excess) reactivity is necessary at the beginning of its operation. In order to keep a critical state in a pressurized water reactor, the positive reactivity is suppressed by a negative reactivity insertion using control rods or chemical shim[1]. Burnable poisons incorporated in nuclear fuel, which have been widely used in commercial light water reactors (LWR) to extend cycle lengths and to increase fuel burnups, are gradually consumed under a neutron irradiation [2]. In most cases, gadolinium (Gd) is used as burnable poison since two isotopes of Gd, ^{155}Gd and ^{157}Gd, have large neutron capture cross sections at the thermal energy (25.3 meV). Hence, it is essential for safe and reliable operations of nuclear power plants to accurately determine the neutron capture cross sections of these nuclides.

For ^{155}Gd and ^{157}Gd, the capture cross sections are much larger than the elastic scattering ones (smaller than 1%) and nearly equal to the total ones in the energy range below 0.1 eV. Many experimental data [3–10] for the total and capture cross sections of ^{155}Gd and ^{157}Gd at the thermal energy are available and summarized in Table 1 in comparison with the latest evaluated values in JENDL-4.0 [11] and ENDF/B-VIII.0 [12] and the compilation data by Mughabghab [13]. As listed in Table 1, the reported values for ^{155}Gd are consistent and in good agreement with the evaluated values in JENDL-4.0 and ENDF/B-VIII.0. However, many of the reported values for ^{157}Gd are inconsistent with the evaluated values.

For ^{157}Gd, the evaluation in JENDL-3 [14] was made based on the data measured by Møller et al. [4]. In 2003, the neutron capture and total cross sections and the resonance parameters in the range from 1 to 300 eV were reported by Leinweber et al. [7]. Some benchmark tests using the data by Leinweber et al. have been performed. The integral experiments at the PROTEUS [15] were reported that the use of the data by Leinweber et al. had the potential to resolve some differences in trends observed for poisoned and poison-free UO_2 rods. Another benchmark test employed several criticality data of low-enriched uranium lattice systems with dissolved gadolinium in the ICSBEP handbook [16]. It reported that the test result had significantly overestimations of the criticalities. In the JENDL-4.0

CONTACT Atsushi Kimura kimura.atsushi04@jaea.go.jp Nuclear Science and Engineering Center, Japan Atomic Energy Agency, 2-4 Shirakata, Tokai-mura, Ibaraki 319-1195, Japan

Table 1. Derived total and capture cross-section data of ^{155}Gd and ^{157}Gd at thermal energy compared to the data in the literature and the evaluations.

Reference	Year	^{155}Gd (kb)	^{157}Gd (kb)	Method
Tattersall et al.[3]	1960	49.8 ± 0.6 [a]	213 ± 2[a]	Pile oscillator
Møller et al.[4]	1960	60.6 ± 0.5 [a]	254 ± 2[a]	TOF
Ohno et. al.[5]	1968	61.9 ± 0.6 [a]	248 ± 4[a]	TOF
Sun et. al.[6]	2003	59.1 ± 4.6[b]	232 ± 14[b]	Prompt gamma-ray
Leinweber et al.[7]	2006	60.7[b]	226[b]	TOF
Noguere et al.[8]	2011	61.9 ± 1.5[b]		Pile oscillator
Choi et. al.[9]	2014	56.7 ± 2.1[a]	239 ± 6[a]	Prompt gamma-ray
Mastromarco et al.[10]	2019	62.2 ± 2.2[b]	239.8 ± 8.4[b]	TOF
JENDL-4.0[11]	2010	60.79[a]	254.1[a]	
		60.74[b]	253.2 [b]	
ENDF/B-VIII.0[12]	2018	60.80[a]	253.9[a]	
		60.74[b]	252.9[b]	
Mughabghab[13]	2018	60.39 ± 0.50 [a]	255.0 ± 0.8[a]	
		60.33 ± 0.50 [b]	254.0 ± 0.8[b]	
This Work		59.4 ± 1.7 [a]	251.9 ± 4.6[a]	TOF
		59.0 ± 2.5 [b]	250.2 ± 5.0[b]	
			247.4 ± 3.9[b]	

[a]Total cross section.
[b]Capture cross section.

evaluation, to reproduce the ICSBEP benchmarks, background cross section was added to the data by Leinweber et al. in the thermal energy range. The background cross section was equal to the difference between the capture cross section of JENDL-3.3 and those of the calculations using the resonance parameters by Leinweber et al. In the ENDF/B-VIII.0 evaluation, the resonance parameters are based on the results reported by Leinweber et al. and the resonance parameters of the 0.0314-eV resonance were adjusted to reproduce the ICSBEP benchmarks. The adjusted parameters are consistent with those reported by Møller et al. As a result, the thermal total cross sections in the latest evaluated files, JENDL-4.0 and ENDF/B-VIII.0, are 254.1 and 253.9 kb, respectively. These values are 11% larger than the result of Leinweber et al.

In 2017, Rocchi et al. [17] performed a sensitivity and uncertainty analysis to investigate the effect of the cross–section data for odd Gd isotopes on the multiplication factor of some LWR fuel assemblies. They reported the importance of the odd Gd isotopes in the criticality evaluation together with the need of a re-evaluation of the neutron capture cross sections. In 2019, Mastromarco et al. [10] reported neutron capture cross section in the energy range from thermal energy to 1 keV and resonance parameters of ^{157}Gd in the energy range from 1 to 307 eV. The reported resonance parameters almost agree with the evaluated libraries but the thermal capture cross section is smaller than the evaluated values by 6%. Thus, another independent measurement is desirable to resolve the discrepancies in the thermal energy range.

In this work, the neutron total and capture cross sections of ^{155}Gd and ^{157}Gd were derived from the data measured in Accurate Neutron-Nucleus Reaction measurement Instrument (ANNRI) at the Materials and Life Science Experimental Facility (MLF) [18] of Japan Proton Accelerator Research Complex (J-PARC). The neutron total cross sections were determined using a well-established neutron-transmission method with Li-glass detectors, and the capture cross sections were determined using a new method by taking the ratio of the detected capture event rate between thin and thick samples with a NaI(Tl) spectrometer.

In this paper, the outlines of the neutron time-of-flight (TOF) experiment facility, ANNRI, and information of the samples are described in Section 2. The total cross-section measurement is presented in Section 3, and the capture cross-section measurement is described in Section 4. Finally, the discussion and summary are given in Sections 5 and 6.

2. Facility and Sample preparation

2.1. ANNRI at J-PARC

The 1-MW pulsed spallation neutron source in the MLF is one of the main experimental facilities within the J-PARC project. A 1-MW proton beam with an intensity of 333 μA accelerated using a 3-GeV rapid cycling synchrotron is injected into a mercury target at a repetition rate of 25 Hz. Intense pulsed neutrons are produced by the spallation reaction in the mercury target. In the MLF, there are three distinctive moderators that employ supercritical hydrogen at 20 K and 1.5 MPa. In the three moderators, a Coupled Moderator (CM) provides the most intense neutron beam. ANNRI is located on No. 04 beam port and uses neutrons from the CM.

In ANNRI, there are two gamma-ray spectrometers and one neutron detector system as shown in Figure 1 [19,20]. In this work, the Li-glass detector system at

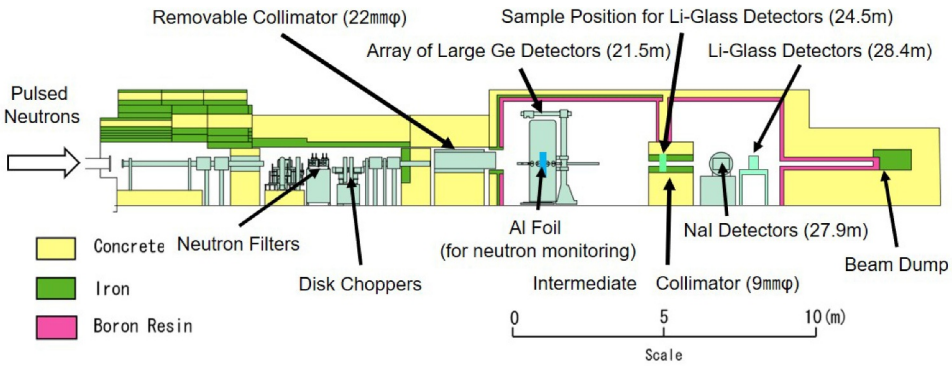

Figure 1. Side view of the ANNRI beamline.

a flight length of 28.4 m and the NaI(Tl) spectrometer installed at a flight length of 27.9 m were used for the total and capture cross-section measurements, respectively. The neutron-beam line of ANNRI consists of neutron notch filters, a disk chopper, collimators, and beam ducts to provide neutrons with optimal quality. The disk chopper made of 95 wt% isotopically enriched $^{10}B_4C$ is used to reduce background due to frame-overlap neutrons originating from one or two previous pulsed neutrons. More details about the ANNRI are given in Ref. [21]. J-PARC was operated at a proton beam power of 206 kW. Throughout the experiment, the number of protons injected into the mercury target was monitored using a current transformer installed at the proton beam-line and was stable within 1.4% in FWHM. During the experiment, for every 2.48 s, the first 58 of 62 proton shots were provided to the MLF and the last four shots were supplied to the other facilities. Start trigger signals for the TOF measurements were produced using a proton beam pulse monitor located in a beam transport tube toward the mercury target.

2.2. Sample preparation

In order to avoid saturation of the yield attributable to self-shielding, very thin samples are required to measure the capture cross sections near the thermal energy region. Enriched gadolinium nitrate, $Gd(NO_3)_3$, was crystalized on a 10-μm^t pure aluminum foil to make thin sample layers with the same size as the Al foil and a thickness of approximately 0.2 μm (or 2 μm), where the gadolinium nitrate layered Al foil was denoted by 'Gd 0.2-μm^t sheet' (or 'Gd 2-μm^t sheet'). Details of the sheet sets are listed in Table 2. For each enriched gadolinium isotope, eight and twelve sheets with nominal thicknesses of 0.2 and 2 μm were prepared, respectively. The area density of each sample sheet was deduced from the area of the Al foil measured with a digital microscope and the weight of the sheet subtracted by that of the Al foil measured with an electronic balance before crystallization. The uncertainty of the area density of each sheet was deduced from the accuracies of the electronic balance and the digital microscope. The averaged area density of each sheet set is written in the third column of Table 2.

The thickness of Gd in each of the produced sample sheets was not uniform. Thus, the influence due to the thickness non-uniformity should be discussed. To estimate this influence, the relative thickness of Gd was measured by using the X-ray fluorescence spectrometry (with a spot size of 50 μm) at the center position and four positions around the corners (i.e. 5 points) on every sheet and the standard deviation of the thickness for each sample sheet set was obtained. The values are shown in the fourth column of Table 2. In the results of the X-ray fluorescence spectrometry, no correlation was found between the measured thickness at the center position and that at the corner positions. In this paper, the thickness of Gd on a sample sheet was assumed to have a truncated normal distribution with no correlation between thickness and position (cf., center and corner on the sample sheet).

To reduce the influence due to thickness non-uniformity, samples stacked with several sheets were used as Gd samples for the experiments. Since it was

Table 2. Characteristics of the ^{155,157}Gd sheet sets.

Name of sheet set	Number of produced sheets	Averaged area density of ^{155}Gd or ^{157}Gd (atoms/b)	Standard deviation of thickness (%)
^{155}Gd 0.2-μm^t sheet	8	6.08×10^{-7}	17.4
^{155}Gd 2-μm^t sheet	12	6.27×10^{-6}	20.4
^{157}Gd 0.2-μm^t sheet	8	5.36×10^{-7}	19.5
^{157}Gd 2-μm^t sheet	12	5.08×10^{-6}	21.2

assumed that the thickness of Gd on the sample sheet had a truncated normal distribution, the thickness of Gd on the stacked sample also had a truncated normal distribution. The area density of the Gd sample was obtained by summing the area densities of the stacked sheets. The dispersion of thickness for the Gd sample was estimated using the deviation of the thickness of the sample sheet set shown in the fourth column of Table 2. The obtained area densities of the Gd sample were used as the mean value in the truncated normal distribution and the dispersion of thickness was used as the variance in the truncated normal distribution. In this paper, the uncertainties of the area density and thickness dispersion were handled separately in the uncertainty analysis.

The sample size was 30 mm × 30 mm and it was large enough to cover the whole neutron beam size. Isotopic compositions of gadolinium in the ^{155}Gd and ^{157}Gd samples were determined by thermal ionization mass spectrometry (TIMS) [22]. The results are shown in Table 3.

Table 3. Isotopic compositions of gadolinium in the Gd samples.

Isotope	^{155}Gd sample (atom%)	^{157}Gd sample (atom%)
^{152}Gd	0.011 ± 0.001	0.003 ± 0.001
^{154}Gd	0.627 ± 0.001	0.038 ± 0.001
^{155}Gd	91.651 ± 0.007	0.293 ± 0.001
^{156}Gd	5.188 ± 0.006	1.684 ± 0.002
^{157}Gd	1.146 ± 0.001	88.325 ± 0.009
^{158}Gd	0.963 ± 0.001	9.089 ± 0.008
^{160}Gd	0.414 ± 0.001	0.568 ± 0.001

3. Neutron total cross section measurements with Li-glass detectors

3.1. Experimental procedure

The experimental procedure was almost in the same manner as that described in Ref. [19,23]. Two types of Li-glass scintillation detectors were utilized for the transmission measurements. The setup of the Li-glass detectors is shown in Figure 2. A ^{6}Li-glass detector manufactured by OKEN was used to obtain the neutron TOF transmission spectra. The scintillator of the detector was GS-20 (^{6}Li enrichment higher than 95%) produced by Saint-Gobain with a dimension of 50 mm × 50 mm and a thickness of 1 mm. Neutrons were detected via the ^{6}Li(n, α)^{3}H reaction. The GS-20 scintillator was coupled to a HAMAMATSU H7195 photomultiplier tube (PMT). The distance from the moderator to the ^{6}Li-glass detector was 28.4 m. Additionally, a ^{7}Li-glass detector was used to determine the background shape due to gamma rays. The scintillator of the ^{7}Li-glass detector was GS-30 (^{7}Li enrichment higher than 99.99%) produced by Saint-Gobain with the same size and chemical component as the GS-20 scintillator. The ^{7}Li-glass detector had the same type of PMT as the ^{6}Li-glass detector. Thus, the neutron sensitivity of the ^{7}Li-glass detector is significantly smaller than that of the ^{6}Li-glass detector due to the small neutron absorption cross section but both sensitivities to gamma rays are almost identical. The ^{7}Li-glass detector was installed on the upstream side of the ^{6}Li-glass detector.

Signals from these detectors were fed into a CAEN V1720 (12bit 250 MHz) module with the CAEN Charge Integration DPP firmware (DPP-CI) [24]. The CAEN V1720 directly digitizes the outputs from the detectors. The DPP-CI calculates the pulse height (PH) data from the total input charge in an integrating window, and records the PH and timing data in 'event-by-event mode.' Further details can be found in the user manual of the DPP-CI [25]. The integrating window width was

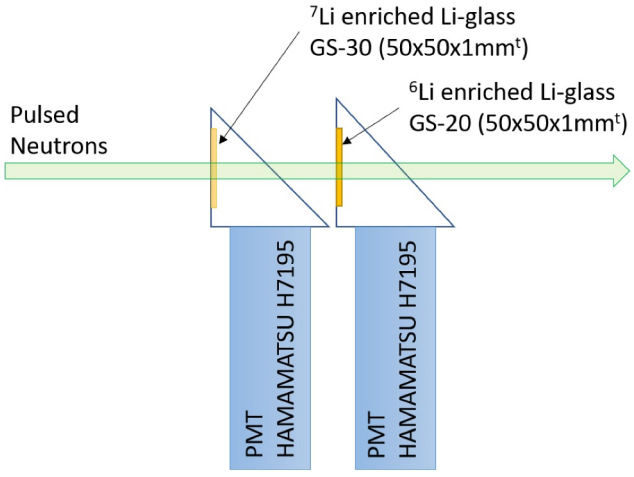

Figure 2. Top view of the setup of Li-glass detectors.

Table 4. Characteristics and measurement time of samples for total cross-section measurements.

Sample name	Materials [b]	Area density of ^{155}Gd or ^{157}Gd (10^{-6}atoms/b)	Dispersion of thickness (%)	Measurement Time (h)
^{155}Gd sample	^{155}Gd 0.2-μm^t sheet × 4	2.46 ± 0.04	8.7	4
^{157}Gd sample	^{157}Gd 0.2-μm^t sheet × 4	2.24 ± 0.04	9.7	6
Al foil sample	Al foil (10 μm^t) × 4	–	–	4
Black resonance[a]	–	–	–	4

[a] With the neutron notch filters of ^{nat}Mn, ^{nat}Co, ^{nat}In, and ^{nat}Ag.
[b] A sample was set on the holder.

set as 1200 ns (300 ch.). The width is long enough compared to the decay time of the GS-20 scintillator (60–110 ns). The dead time per event was set as 1264 ± 4 ns (316 ± 1 ch.) using the trigger holdoff function of the DPP-CI.

A lead block with a thickness of 87.5 mm was placed on the neutron beam line, in order to reduce the dead time of the Li-glass detectors caused by intense gamma rays from the moderator.

In the total cross-section measurements, the 'Gd 0.2-μm^t sheets' were quadruply stacked and the stacked sheets were used as a Gd sample with an effective thickness of 0.8 μm. The area density and the measurement time of each sample is summarized in Table 4. These samples were placed in the intermediate collimator at a flight length of 24 m. A measurement with four Al foils with a thickness of 10 μm was also carried out to estimate the 'sample out' conditions. The black resonance technique was applied using the neutron notch filters of ^{nat}Mn, ^{nat}Co, ^{nat}In, and ^{nat}Ag to normalize the background shape due to gamma rays. TOF parameters, flight length and offset time from the electric trigger signal to the gamma flash (i.e. t_0) were determined using unsaturated resonances of the neutron notch filters. Moreover, to estimate relative neutron intensities, an Al foil with a thickness of 20 μm was set at the sample position of the array of large Ge detectors which is installed at the upstream side of the Li-glass detectors [26], and prompt gamma-rays from the ^{27}Al(n, γ) reaction were measured with the Ge detectors at the same time as the measurements listed in Table 4 .

3.2. Data analysis

3.2.1. Pulse height spectra

The PH spectra of the ^{157}Gd sample with the ^{6}Li-glass and ^{7}Li-glass detectors are shown in Figure 3. The events due to the ^{6}Li(n, α)^{3}H reaction (around 2600 ch.), double-hit (around 5200 ch.) and triple-hit (around 7800 ch.) are clearly observed in the PH spectrum of the ^{6}Li-glass detector. Since GS-30 contains a slight amount of ^{6}Li (less than 0.01%), the ^{7}Li-glass detector has weak sensitivity to neutron, and the spectrum measured by the ^{7}Li-glass detector also exhibits peaks due to the ^{6}Li(n, α)^{3}H reaction. A lower discrimination gate at 1700 ch. was applied to derive TOF spectra, as shown in Figure 3.

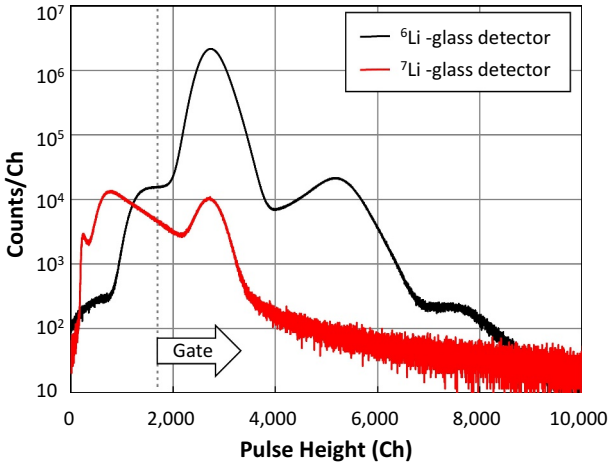

Figure 3. Pulse height spectra of the ^{157}Gd sample measured with the ^{6}Li-glass and ^{7}Li-glass detectors.

3.2.2. Raw TOF spectra

Figure 4 displays the gated TOF spectra of the ^{155}Gd, ^{157}Gd, and Al samples measured with the ^{6}Li-glass and ^{7}Li-glass detectors. Each TOF spectrum was normalized with the number of proton beam shots. The broad peak around 15–35 ms is ascribed to the thermalized neutron bump made by the liquid hydrogen moderator. The gamma-ray backgrounds deduced from the TOF spectra with the ^{7}Li-glass detector were smaller than the neutron TOF spectra with the ^{6}Li-glass detector by two orders of magnitude.

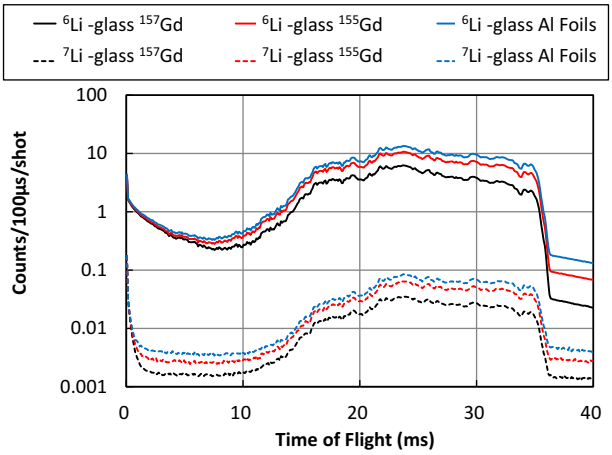

Figure 4. Gated TOF spectra of the ^{155}Gd, ^{157}Gd, and Al samples measured with the ^{6}Li-glass and ^{7}Li-glass detectors. Each TOF spectrum was normalized with the number of proton beam shots.

3.2.3. Dead time correction

Dead time corrections were made with the traditional non-paralyzable dead-time model [27]. The dead time per event was set as 1264 ± 4 ns (316 ± 1 ch.). The calculated dead time correction factors for the ^{155}Gd, ^{157}Gd, and Al samples measured with the ^{6}Li-glass detector are shown in Figure 5. The dead time for the ^{7}Li-glass detector was negligibly small in this experiment. The uncertainties of the correction were calculated from the uncertainty of the dead time per event (0.32%) and the statistic uncertainty of the total measured events in the period of the dead time. The influences of the double-hit and triple-hit events were also corrected in this dead time correction.

3.2.4. Frame overlap background and constant background

During the experiment, the first 58 of every 62 shots were provided to MLF and the other shots were delivered to the other facilities. Thus, every 2.48 s, a distinct TOF spectrum with a broad time range (to 200 ms, different from that with normal 40 ms) was obtained. The wide range TOF spectrum of the ^{157}Gd sample measured with the ^{6}Li-glass detector, is shown up to 80 ms in Figure 6. As shown in Figure 6, the disk chopper was closed in the TOF range from 36 to 73 ms. The tail of the previous neutron pulse was observed in the wide range TOF spectrum after 40 ms. The effect of the disk chopper (described in Appendix) can be seen in the tail of the previous neutron pulse. After 73 ms (instead of 33 ms in the normal TOF) the disk chopper was opened again. The counts suddenly increase by an order of magnitude. Nonetheless, in this analysis, the TOF data before 30 ms was used for the spectrum analysis, and the influence due to the re-open of the disk chopper was not estimated.

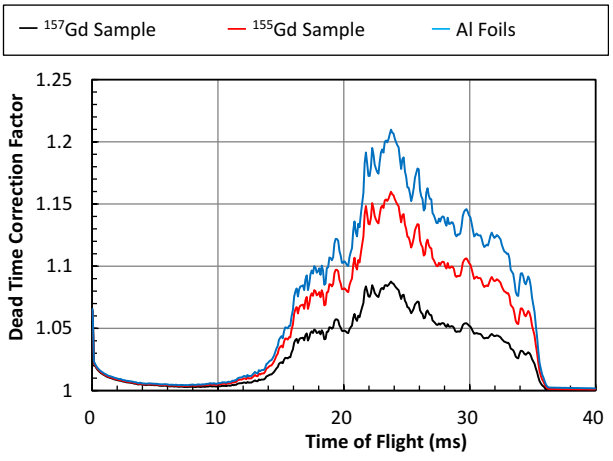

Figure 5. Dead time correction factors for the ^{155}Gd, ^{157}Gd and Al samples in the measurements with the ^{6}Li-glass detector.

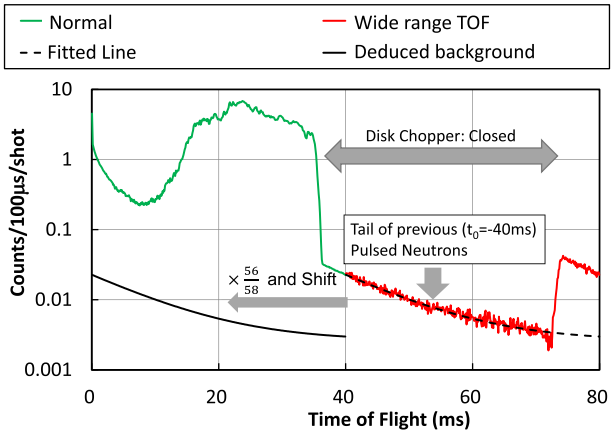

Figure 6. Wide range TOF spectrum after 40 ms and normal TOF spectrum in comparison with the fitted result and the deduced frame overlap and constant backgrounds. The TOF spectra are results of the ^{157}Gd sample with the ^{6}Li-glass detector.

The frame overlap background and constant background in the normal TOF range earlier than 30 ms were deduced by fitting the following equation to this wide range TOF spectrum in the TOF region from 40 ms to 70 ms [28]:

$$F(t) = \alpha \times \exp(-\frac{t}{t_c}) + \beta, \qquad (1)$$

where t is the TOF in ms and α, β and t_c are fitting parameters. The fitted curve corresponding to the background spectrum is also displayed in Figure 6. The obtained time constant t_c was about 11 ms. The first two of 58 proton beam shots do not have any influence of the preceding ones on the frame overlap background because four proton shots before the first two ones were not delivered to MLF. Thus, the frame overlap background and constant background, $B_{F+C}(t)$, was deduced by the following equation in the TOF range between 0 and 30 ms,

$$B_{F+C}(t) = \frac{56}{58} \times \alpha \times \exp(-\frac{t + 40\text{ms}}{t_c}) + \beta. \qquad (2)$$

The determined background is also shown in Figure 6. This background estimation was applied to each TOF spectrum. In this step, uncertainties of this background subtraction were deduced from the uncertainties of the fitted parameters.

3.2.5. Gamma-ray background

Background events due to detected gamma-rays were derived from the TOF spectra measured with the ^{7}Li-glass detector. In order to correct the difference in the gamma-ray detection efficiency between the ^{6}Li-glass and ^{7}Li-glass detectors, the black resonance technique was applied to normalize the TOF spectra measured with the ^{7}Li-glass detector at the four dips by ^{55}Mn, ^{59}Co, ^{115}In

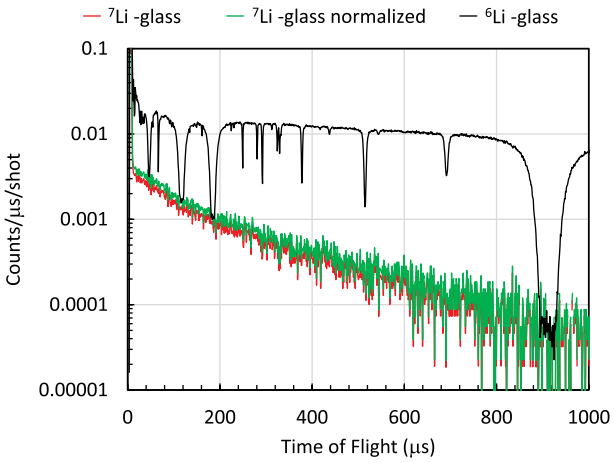

Figure 7. TOF spectra of the ^{6}Li-glass and ^{7}Li-glass detectors before and after normalization. The TOF spectra are results of the Blank sample with the neutron notch filters of ^{nat}Mn, ^{nat}Co, ^{nat}In, and ^{nat}Ag.

and ^{109}Ag. Figure 7 shows the TOF spectra of the ^{6}Li-glass detector and those of the ^{7}Li-glass detector before and after normalization. The deduced normalization factor was 1.16 ± 0.04. Uncertainties due to this background subtraction were deduced from the uncertainties of the normalization factor and the statistical uncertainties. The deduced uncertainties were very small, since the spectrum with the ^{7}Li-glass detector was much smaller than that with the ^{6}Li-glass detector in the neutron energy range below 1 eV (TOF range after 2 ms), as presented in Figure 4 .

The deduced background of each sample is shown in Figure 8 in comparison to the TOF spectrum of each sample measured with the ^{6}Li-glass detector after the frame overlap and constant backgrounds were removed. As shown in Figure 8, the obtained background is less than 1% relative to the TOF spectrum

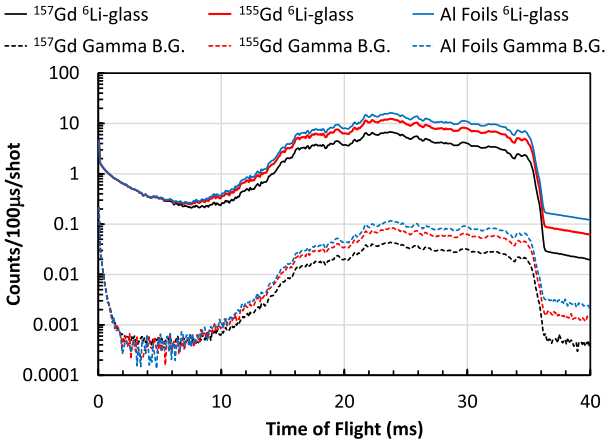

Figure 8. Gamma-ray background spectra of the ^{155}Gd, ^{157}Gd, and Al samples and TOF spectra with the ^{6}Li-glass detector after the frame overlap and constant backgrounds were removed.

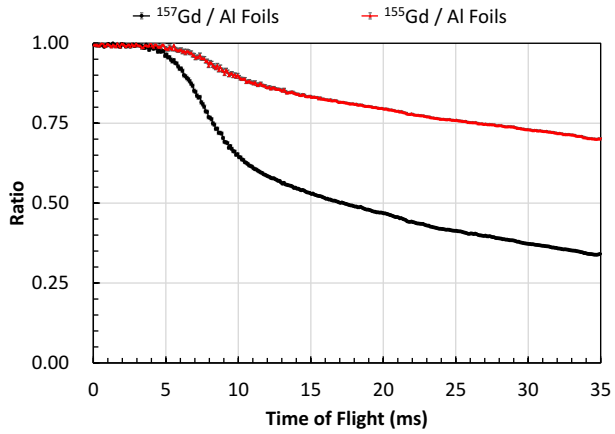

Figure 9. Transmission ratios of the ^{155}Gd and ^{157}Gd samples to the Al sample. The error bars represent the statistical uncertainties.

with the ^{6}Li-glass detector in the neutron energy range below 0.1 eV (over 6.5 ms in TOF). The net neutron TOF spectra of the ^{155}Gd, ^{157}Gd, and Al samples were obtained by subtracting the normalized TOF spectra with the ^{7}Li-glass detector from the TOF spectra with the ^{6}Li-glass detector.

3.2.6. Transmission ratio

In the experiment, to estimate the relative neutron intensities, an Al foil with a thickness of 20 μm was set at the sample position of the array of large Ge detectors and prompt gamma-rays from the ^{27}Al(n, γ) reaction were measured at the same time as the measurements with the Li-glass detectors. The number of events whose gamma-ray energies were over 2000 keV and neutron energies were smaller than 0.1 eV was used to eliminate the strong decay gamma rays from ^{28}Al (1778 keV). Relative neutron intensity per proton beam shot for each sample was derived by dividing the number of the gated gamma-rays by the number of proton beam shots in the measurement. Due to neutron intensity differences, correction factors were deduced by taking the ratio between the deduced relative neutron intensities. The correction factors were 1.0063 ± 0.0002 for the ratio of the ^{155}Gd sample to the Al sample and 1.0069 ± 0.0002 for the ^{157}Gd sample. Uncertainties due to the neutron intensity normalization were calculated from those of these factors. The obtained transmission ratios are shown in Figure 9 with the uncertainties.

3.2.7. Cross section calculation

The thickness of Gd on each Gd sample was given by a truncated normal distribution. The mean value of the distribution was the area density of the Gd sample and the variance was the thickness

dispersion. The transmission ratios, $R(E_n)$, for the ^{155}Gd and ^{157}Gd samples were calculated with the following equation:

$$R(E_n) = \int_a^b \exp(-\sigma_{tot}(E_n) \times N_{Gd} \times x) \times f(x;\mu,s,a,b)dx, \quad (3)$$

where $\mu = 1$, $a = 0$, $b = 2$, $\sigma_{tot}(E_n)$ is the total cross sections of the Gd samples, s is the thickness standard deviation of the Gd samples described in the fourth column of Table 4, N_{Gd} is area density of the Gd sample described in the third column of Table 4 and $f(x;\mu,s,a,b)$ is a probability density function of the truncated normal distribution with mean μ and variance s^2 within the region from a to b. The total cross sections for the ^{155}Gd and ^{157}Gd samples were deduced using Equation (3) and the transmission ratios shown in Figure 9.

The uncertainty related to the sample mass was propagated from the uncertainties of the area density with Equation (3). The uncertainty due to thickness non-uniformity (i.e. the influence of the thickness dispersion) was assumed from the difference between the results with and without the truncated normal distribution in Equation (3). If the sample was tilted, the area density of the Gd sample would be underestimated. The sample setting accuracy was estimated as less than 5 degrees. The uncertainty due to sample setting was deduced from the difference between the results with and without the tilt of the sample.

3.3. Results

The deduced total cross sections for the ^{155}Gd and the ^{157}Gd samples include influences of the sample impurities. However, the total cross sections of ^{155}Gd and ^{157}Gd are much larger than those of the other Gd isotopes in the thermal region. Hence, in the present analysis, only the influence of ^{155}Gd and ^{157}Gd were considered. The influence of the ^{155}Gd contamination in the ^{157}Gd sample was negligible since the ^{155}Gd contamination was less than 0.3% and the total cross section of ^{157}Gd is 4 times larger than that of ^{155}Gd. The derived total cross section of ^{157}Gd is shown in Figure 10 together with the evaluated values in JENDL-4.0 and ENDF/B-VIII.0. On the other hand, the ^{157}Gd contamination in the ^{155}Gd sample is not negligible. The contribution of the ^{157}Gd contamination was subtracted from the total cross section of ^{155}Gd sample using the deduced total cross section of ^{157}Gd. The derived total cross section of ^{155}Gd is shown in Figure 11.

In this analysis, the statistical uncertainty and the uncertainties due to the dead time correction (in Section 3.2.3.), the frame overlap subtraction (in Section 3.2.4.), the gamma-ray background subtraction (in Section 3.2.5.), the neutron intensity normalization (in Section 3.2.6.), the sample mass, the sample setting accuracy, the thickness non-uniformity (in Section 3.2.7.), and the subtraction of ^{157}Gd contribution were considered. The uncertainty due to the ^{157}Gd contribution was derived from the uncertainties of the abundance and the deduced ^{157}Gd total cross section. Some of the estimated uncertainties are shown in Figures 12 and 13. The details of these uncertainties at the thermal energy are summarized in Table 5. In the total cross section at the thermal energy, the main component of the uncertainty comes from the statistical uncertainty and the systematic uncertainties related to the area density of Gd.

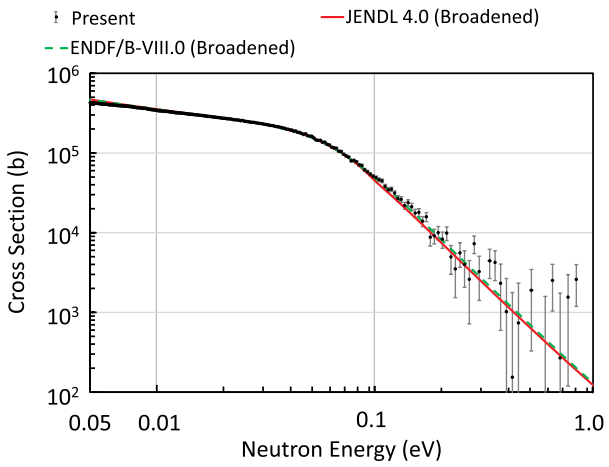

Figure 10. Derived total cross section of ^{157}Gd compared to the evaluated values of JENDL-4.0 and ENDF/B-VIII.0 at the temperature of 300 K (broadened with the resolution function of ANNRI [29]). The error bars represent the statistical uncertainties.

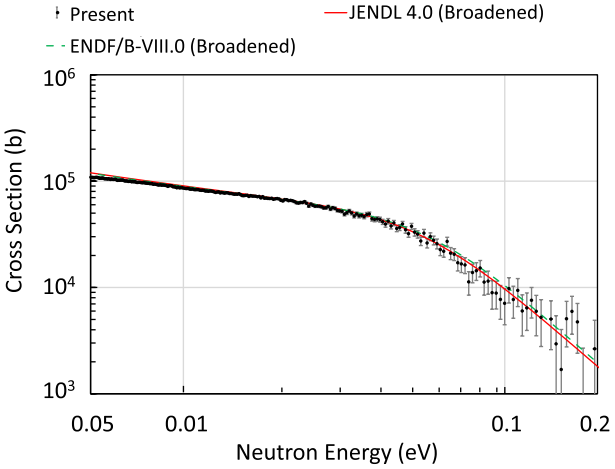

Figure 11. Derived total cross section of ^{155}Gd compared to the evaluated values of JENDL-4.0 and ENDF/B-VIII.0 at the temperature of 300 K (broadened with the resolution function of ANNRI [29]). The error bars represent the statistical uncertainties.

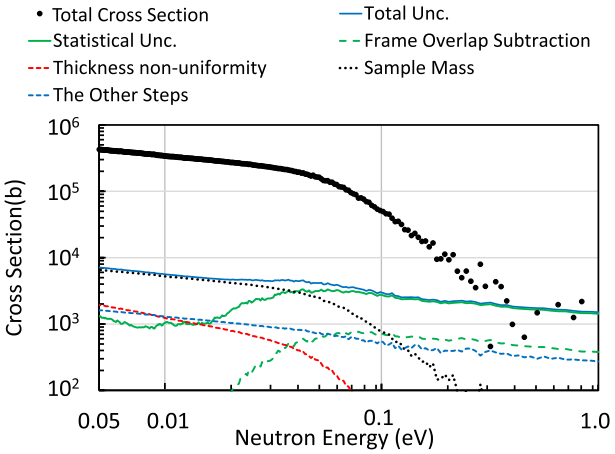

Figure 12. Derived total cross section of ^{157}Gd, and uncertainties of the cross section (total and statistical uncertainties, and uncertainties due to frame overlap subtraction, thickness non-uniformity of the sample and sample mass). The other uncertainties, not shown explicitly but considered, are those due to dead time correction, neutron intensity normalization, gamma-ray background subtraction and sample setting.

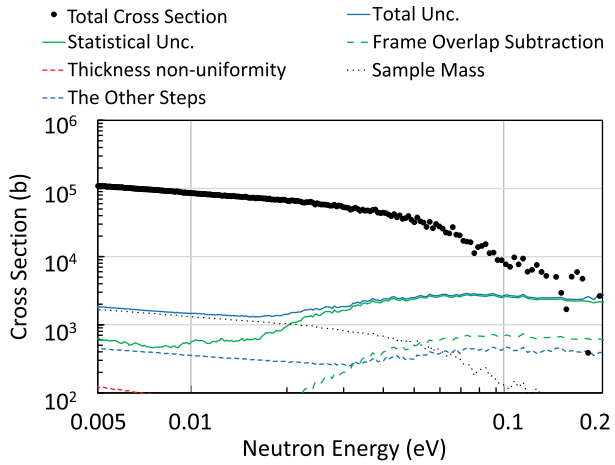

Figure 13. Derived total cross section of ^{155}Gd, and uncertainties of the cross section (total and statistical uncertainties, and uncertainties due to frame overlap subtraction, thickness non-uniformity of the sample and sample mass). The other uncertainties, not shown explicitly but considered, are those due to dead time correction, neutron intensity, gamma-ray background subtraction, sample setting condition and subtraction of ^{157}Gd contribution.

4. Neutron capture cross section measurement with the NaI(Tl) spectrometer

4.1. Experimental procedure

The NaI(Tl) spectrometer in ANNRI [30,31] was used in the capture cross-section measurement. The setup of the NaI(Tl) spectrometer is shown in Figure 14. The NaI(Tl) spectrometer consists of two different-sized NaI(Tl) detectors each of which is surrounded by plastic scintillators. The large-sized NaI(Tl) detector, with a diameter of 330 mm and a length of 203 mm, is placed at the angle of 90 degrees with respect to the neutron-beam line and the small-sized NaI(Tl) detector, with a diameter of 203 mm and a length of 203 mm, is placed at the angle of 125 degrees. If necessary, the detector at 125 degrees is used to reduce the effects of angular distributions of capture gamma rays from resonances with the orbital angular momentum, $l > 0$. The plastic scintillators are used to eliminate events triggered mainly by cosmic rays. The detectors are shielded by lead, cadmium, borated polyethylene and borated rubber. In addition, in order to shield the detector from neutrons scattered at the sample, enriched ^{6}LiH powder enclosed in an Al

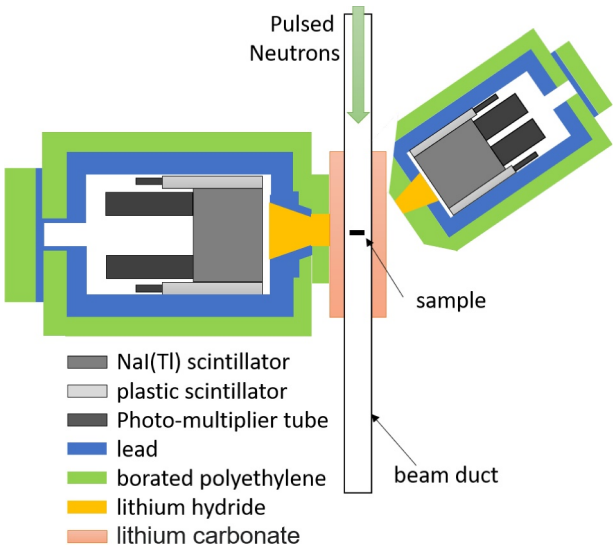

Figure 14. Top view of the setup of the NaI(Tl) spectrometer in ANNRI. The large- and small-sized NaI(Tl) detectors are placed at the left and right sides of the beam duct.

Table 5. Details of uncertainties for the derived total cross section of ^{155}Gd and ^{157}Gd at the thermal energy.

	^{155}Gd (kb)	^{157}Gd (kb)
Derived cross section	59.4 ± 1.7	251.9 ± 4.6
Statistical uncertainty	1.4	2.2
Dead time correction	0.1	0.1
Frame overlap subtraction	0.1	0.2
Gamma-ray background subtraction	< 0.1	< 0.1
Neutron intensity normalization	0.1	0.1
Sample mass	0.9	3.9
Sample setting accuracy	0.2	1.0
Thickness non-uniformity	0.1	0.7
^{157}Gd contribution	< 0.1	–

Table 6. Characteristics and measurement time of samples for the capture cross-section measurements.

Sample name	Materials [b]	Area density of ^{155}Gd or ^{157}Gd (10^{-6}atoms/b)	Dispersion of thickness (%)	Measurement Time (h)
^{155}Gd 0.6-μm^t sample	^{155}Gd 0.2-μm^t sheet × 3	1.71 ± 0.03	10.1	4
^{155}Gd 10-μm^t sample	^{155}Gd 2-μm^t sheet × 5	2.94 ± 0.04	9.0	4
^{157}Gd 0.6-μm^t sample	^{157}Gd 0.2-μm^t sheet × 3	1.72 ± 0.03	11.3	5
^{157}Gd 1.2-μm^t sample	^{157}Gd 0.2-μm^t sheet × 6	3.22 ± 0.04	8.0	15
^{157}Gd 20-μm^t sample	^{157}Gd 2-μm^t sheet × 10	49.6 ± 0.5	6.7	16
Al sample	Al Foil (10 μm^t) × 5	–	–	4
Blank sample	–	–	–	4
Au sample	Au foil (20 mmϕ, 10 μm^t)	–	–	1

[a] Sample was sealed in the FEP bag and fixed on the holder.

container is placed in front of the detectors and the carbon fiber beam duct around the sample position was covered with enriched $^6Li_2CO_3$ powder enclosed in a polytetrafluoroethylene container of a hollow cylindrical shape. The details of the NaI(Tl) spectrometer are presented in Ref. [32]. In the present experiment, there is no need to consider the angular distribution effect of capture gamma rays, since the effect is canceled out, by taking the ratio of the capture yield of a thin sample to that of a thick sample. Therefore, the NaI(Tl) spectrometer at 90 degrees was only used.

Three HAMAMATSU R877 PMTs were attached to the NaI(Tl) scintillator at 90 degrees. The sum of the dynode signals was fed into the multiple-event time digitizer, a FAST ComTec MCS6. The pulse-width data digitized by the module were converted into the PH in an offline data analysis. A lower discrimination at 800 keV was applied to eliminate the influence of 478-keV gamma-rays from the ^{10}B(n, $\alpha\gamma$) reaction. Further description in detail of this methodology (Pulse Width Analysis technique) is described by Katabuchi et al [33].

Five Gd samples, which consisted of different numbers of Gd sheets stacked, were used in the measurements with the NaI(Tl) spectrometer, as shown in Table 6. The sample name, area density and measuring time for each stacked sample were summarized in the table. Each sample was sealed in a bag of fluorinated ethylene propylene (FEP) films and attached to a sample holder. The sample holder made of polytetrafluoroethylene (PTFE) and Al was inserted with the sample at the flight length of 27.9 m. For the background estimation, measurement with the Al foil sample and an FEP bag without a sample ('Blank sample') was also carried out. To estimate the relative neutron intensities, an Al foil with a thickness of 10 μm was set at the sample position of the array of large Ge detectors which is the upstream side of the NaI(Tl) spectrometer, and measurements with the Ge detectors were conducted simultaneously with the NaI(Tl) spectrometer. A measurement with a gold foil with a thickness of 10 μm and a diameter of 20 mm was also performed to determine TOF parameters.

4.2. Analysis methodology

An innovative method was developed and applied to enhance the reliability of the capture cross sections of ^{155}Gd and ^{157}Gd. In this analysis, the capture cross section was obtained by taking the ratios of the detected capture event rates between the thin and thick samples described in Table 6. In the neutron energy range below 0.1 eV, the capture cross sections of ^{155}Gd and ^{157}Gd are much larger than the elastic scattering cross sections of ^{155}Gd and ^{157}Gd, and the capture and elastic scattering cross sections of the other nuclides in the samples, for example, aluminum and the other Gd isotopes. The influence of scattered neutrons and capture events due to the other nuclides was negligible. In this case, when the sizes of the samples are large enough in comparison with the neutron beam size, the detected capture event rate of one of ^{155}Gd or ^{157}Gd samples, $Y_{Gd}(E_n)$, is described as follows:

$$Y_{Gd}(E_n) = \phi(E_n) \times (1 - \exp(-(\sum_x \sigma_{cap\,x}(E_n) \times N_x))) \times C_{cap}(E_n), \quad (4)$$

$$C_{cap}(E_n) = \sum_x \left(\frac{\sigma_{cap\,x}(E_n) \times N_x}{\sum_y (\sigma_{cap\,y}(E_n) \times N_y)} \times \int G_x(E_n, E_g) \times k_{det}(E_g) \times k_{sam}(E_g) dE_g \right), \quad (5)$$

where $\phi(E_n)$ is the neutron spectrum, $\sigma_{cap\,x}(E_n)$ is the capture cross section of x, the suffixes x and y represent ^{155}Gd or ^{157}Gd, N_x is the area density of x, $G_x(E_n, E_g)$ is the emitted gamma-ray spectrum per neutron capture event by x, E_n and E_g denote the neutron and gamma-ray energies, $k_{det}(E_g)$ is the gamma-ray detection efficiency, and $k_{sam}(E_g)$ is the escape efficiency of gamma-rays from the sample (sample-dependent value). The term of $\phi(E_n) \times (1 - \exp(-(\sum_x \sigma_{cap\,x}(E_n) \times N_x)))$ in Equation (4) indicates the capture reaction rate in the sample, and $C_{cap}(E_n)$ represents the detected counting rate per neutron capture event. The term of

$\frac{\sigma_{cap\,x}(E_n)\times N_x}{\sum_y \sigma_{cap\,y}(E_n)\times N_y}$ in Equation (5) indicates the ratio of capture events by x to the total capture events in the sample.

In the experiments, since the lower discrimination at 800 keV was applied and the thicknesses of the samples were thin enough, as shown in Table 6, the influence of gamma-ray attenuation in the samples was negligibly small, i.e. $k_{sam}(E_g) = 1$. Equation (5) is rewritten as

$$C_{cap}(E_n) = \frac{\sum_x \sigma_{cap\,x}(E_n) \times N_x \times \int G_x(E_n, E_g) \times k_{det}(E_g) dE_g}{\sum_y \sigma_{cap\,y}(E_n) \times N_y}. \quad (6)$$

Since the thin and thick samples have the same isotopic compositions, area densities are given by

$$N_{x\,thick} = p_{sample} \times N_{x\,thin}. \quad (7)$$

Here, the suffixes *thin* and *thick* mean the thin and thick samples, and p_{sample} is the mass ratio of the thick to thin samples. Using Equations (6) and (7), the following relationship is derived:

$$C_{cap\,thick}(E_n) = \frac{\sum_x \sigma_{cap\,x}(E_n) \times N_{x\,thick} \times \int G_x(E_n, E_g) \times k_{det}(E_g) dE_g}{\sum_y \sigma_{cap\,y}(E_n) \times N_{y\,thick}}$$

$$= \frac{\sum_x \sigma_{cap\,x}(E_n) \times p_{sample} \times N_{x\,thin} \times \int G_x(E_n, E_g) \times k_{det}(E_g) dE_g}{\sum_y \sigma_{cap\,y}(E_n) \times p_{sample} \times N_{y\,thin}}$$

$$= \frac{\sum_x \sigma_{cap\,x}(E_n) \times N_{x\,thin} \times \int G_x(E_n, E_g) \times k_{det}(E_g) dE_g}{\sum_y \sigma_{cap\,y}(E_n) \times N_{y\,thin}}$$

$$= C_{cap\,thin}(E_n). \quad (8)$$

From Equations (4) and (8), the ratio of the detected capture event rate of the thin sample to that of the thick sample, $R(E_n)$, is obtained as follows:

$$R(E_n) = \frac{Y_{Gd\,thin}(E_n)}{Y_{Gd\,thick}(E_n)}$$

$$= \frac{\phi(E_n) \times (1 - \exp(-(\sum_x \sigma_{cap\,x}(E_n) \times N_{x\,thin}))) \times C_{cap\,thin}(E_n)}{\phi(E_n) \times (1 - \exp(-(\sum_y \sigma_{cap\,y}(E_n) \times N_{y\,thick}))) \times C_{cap\,thick}(E_n)}$$

$$= \frac{1 - \exp(-(\sum_x \sigma_{cap\,x}(E_n) \times N_{x\,thin}))}{1 - \exp(-(\sum_y \sigma_{cap\,y}(E_n) \times N_{y\,thick}))}. \quad (9)$$

As shown in Equation (9), the neutron spectrum and the detection efficiency of the spectrometer are canceled out, and the absolute capture cross section can be derived.

For the ^{157}Gd samples, the influence of the ^{155}Gd contamination is negligible. Equation (9) is simply rewritten by

$$R_{157}(E_n) = \frac{1 - \exp(-\sigma_{cap\,157}(E_n) \times N_{157\,thin})}{1 - \exp(-\sigma_{cap\,157}(E_n) \times N_{157\,thick})}. \quad (10)$$

On the other hand, in the analysis for the ^{155}Gd samples, the influence of the ^{157}Gd contamination is not negligible and Equation (9) is expressed as follows:

$$R_{155}(E_n) = \frac{1 - \exp(-(\sigma_{cap\,155}(E_n) \times N_{155\,thin} + \sigma_{cap\,157}(E_n) \times N_{157\,thin}))}{1 - \exp(-(\sigma_{cap\,155}(E_n) \times N_{155\,thick} + \sigma_{cap\,157}(E_n) \times N_{157\,thick}))}$$

$$= \frac{1 - \exp(-\sigma_{sample}(E_n) \times N_{155\,thin})}{1 - \exp(-\sigma_{sample}(E_n) \times N_{155\,thick})}, \quad (11)$$

$$\sigma_{sample}(E_n) = \sigma_{cap\,155}(E_n) + \sigma_{cap\,157}(E_n) \times r_{157/155}, \quad (12)$$

$$r_{157/155} = \frac{N_{157\,thick}}{N_{155\,thick}} = \frac{N_{157\,thin}}{N_{155\,thin}}. \quad (13)$$

Here, $r_{157/155}$ is the isotopic ratio of ^{157}Gd to ^{155}Gd in the ^{155}Gd samples.

As discussed in Section 3.3., by assuming the truncated normal distribution for thickness non-uniformity, Equations (10) and (11) are transformed into the following:

$$R_{157}(E_n) = \frac{1 - \int_a^b \exp(-\sigma_{tot\,157}(E_n) \times N_{157\,thin} \times x) \times f(x; \mu, s_{157\,thin}, a, b) dx}{1 - \int_a^b \exp(-\sigma_{tot\,157}(E_n) \times N_{157\,thick} \times x) \times f(x; \mu, s_{157\,thick}, a, b) dx}, \quad (14)$$

$$R_{155}(E_n) = \frac{1 - \int_a^b \exp(-\sigma_{sample}(E_n) \times N_{155\,thin} \times x) \times f(x; \mu, s_{155\,thin}, a, b) dx}{1 - \int_a^b \exp(-\sigma_{sample}(E_n) \times N_{155\,thick} \times x) \times f(x; \mu, s_{155\,thick}, a, b) dx}, \quad (15)$$

where $\mu = 1$, $a = 0$, $b = 2$, $s_{155\,thin}$, $s_{155\,thick}$, $s_{157\,thin}$ and $s_{157\,thick}$ are the thickness standard deviations of the ^{155}Gd and ^{157}Gd samples, as shown in the fourth column of Table 6. Finally, the neutron capture cross sections of ^{157}Gd and ^{155}Gd were determined using Equations (14) and (15).

4.3. Data analysis

4.3.1. Raw TOF spectra

As described in Section 4.2., since the detection efficiencies of gamma-rays from neutron capture reactions were canceled out by taking ratios of the detected capture event rates, the pulse height weighting technique [34] was not applied in this analysis. Figure 15 shows the TOF spectra for the ^{155}Gd and ^{157}Gd samples along with those for the Al sample and

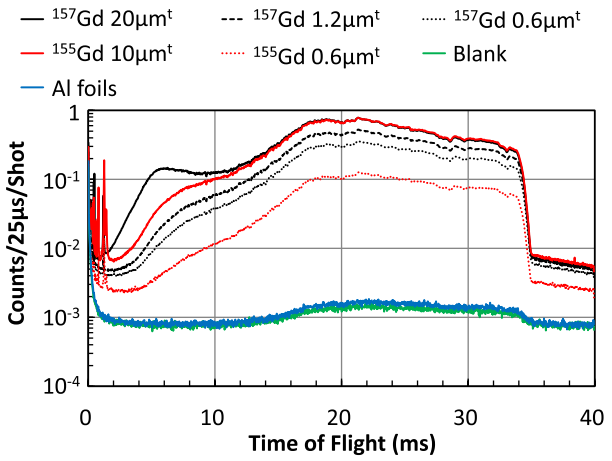

Figure 15. TOF spectra for the ^{155}Gd and ^{157}Gd samples along with those for the Al sample and the Blank sample. Each TOF spectrum was normalized with the number of proton beam shots. The data were processed using a 25-μs time bin.

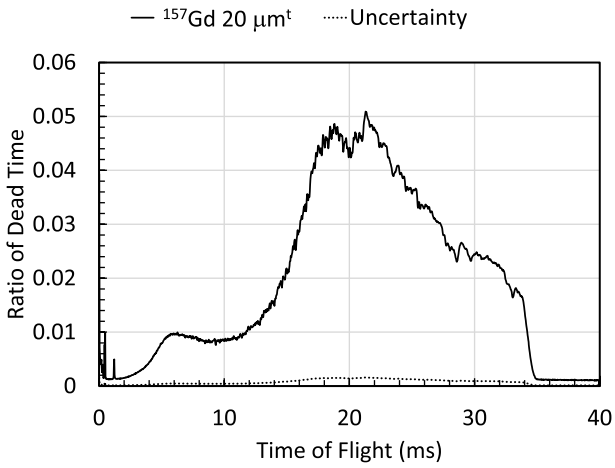

Figure 16. Calculated dead time ratio for the ^{157}Gd 20-μm^t sample and its uncertainty.

the Blank sample. Each TOF spectrum was normalized with the number of proton beam shots. The data were processed with a 25-μs time bin and the lower discrimination level of 800 keV. As shown in Figure 15, event rates for the Gd samples were much higher than those for the Al and Blank samples in the TOF region after 6 ms (in the neutron energy range below 0.1 eV).

4.3.2. Dead time correction

In the pulse width analysis technique, the total dead time of the entire system is dominated by the pulse width of the PMT anode signal. The dead time of the system can be calculated in an offline data analysis. The dead time ratio, $P_{dt}(i)$, was calculated for each TOF channel, i, as follows:

$$P_{dt}(i) = \frac{N_{ds}(i)}{N_{shot} \times t}, \tag{16}$$

where $N_{ds}(i)$ is the total time of the system being in the detecting state in the bin-channel i, N_{shot} is the number of neutron shots, and Δt is the TOF bin width ($=$ 25 μs). The detecting state of the system is defined as the state that the input signal level is higher than the threshold level for the pulse width analysis technique. Details of this methodology are described by Katabuchi et al [33].

The TOF dependence of the calculated dead time ratio for the ^{157}Gd 20-μm^t sample (the highest event rate sample) is shown in Figure 16. The deduced dead time ratio was smaller than 5.1%. The uncertainty of the dead time ratio for each sample was calculated from the statistical uncertainty of the time of the system being in the detecting state per bin width, $\frac{N_{ds}(i)}{\Delta t}$. The deduced uncertainty for the ^{157}Gd 20-μm^t sample is also shown in Figure 16.

Dead time correction factors, $R_{dtc}(i)$, can be obtained with the following equation:

$$R_{dtc}(i) = \frac{1}{(1 - P_{dt}(i))}. \tag{17}$$

The deduced dead time correction factor was smaller than 1.053 for the ^{157}Gd 20-μm^t sample. The uncertainties of the dead time correction factors were also calculated using Equation (17) and the uncertainties of the dead time ratio. The obtained uncertainties were smaller than 0.2%.

4.3.3. Background subtraction

The following backgrounds were considered in the analysis:

(1) the background caused by frame overlap neutrons;
(2) the constant background;
(3) the sample-independent (Blank sample) background;
(4) the background due to the Al foils in the Gd samples;
(5) the background due to neutrons scattered by Gd nuclei and captured by other nuclei except for Gd.

In the neutron energy range below 1 eV (TOF range over 2 ms), the elastic scattering cross sections of ^{155}Gd and ^{157}Gd are much smaller than the capture cross sections. Moreover, most of the scattered neutrons by the Gd samples were captured via the ^{6}Li(n, α)^{3}H reaction in the ^{6}LiCO$_3$ shield and this reaction does not emit gamma rays. Therefore, the last item (5), the background due to the neutrons scattered by Gd nuclei and captured by other nuclei except for Gd (such as the Al foils, the carbon beam duct, the detectors, and so on), was negligible.

The frame overlap background and the constant background for the items (1) and (2) were deduced using the broad range TOF spectrum every 58 shots. In the analysis with the NaI(Tl) spectrometer, the influence of the disk chopper on the frame overlap

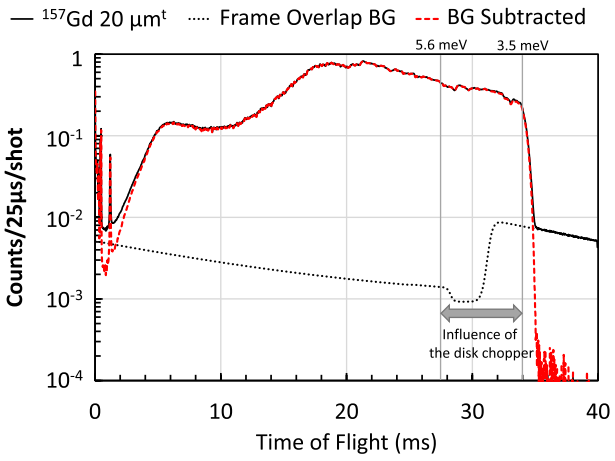

Figure 17. Determined frame overlap background and constant background in comparison with the TOF spectrum before and after subtracting the backgrounds. The TOF spectra are results of the ^{157}Gd 20-μm^t sample.

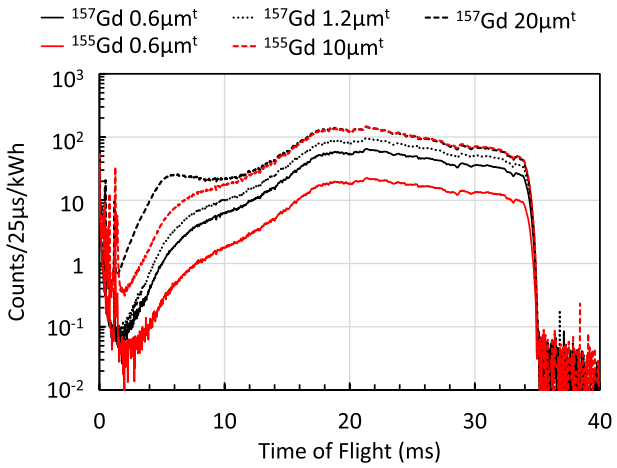

Figure 18. Net TOF spectrum for the ^{155}Gd and ^{157}Gd samples. The TOF spectra were normalized to the proton beam power of 1 kWh at the measurement of the ^{157}Gd 20-μm^t sample.

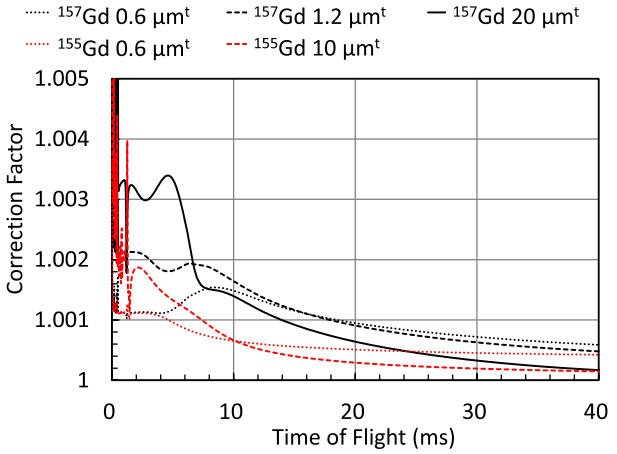

Figure 19. Multiple scattering correction factors for the ^{155}Gd and ^{157}Gd samples.

background appears between 27.5 and 34 ms in TOF. In order to expand the TOF spectra up to 34 ms (3.5 meV in neutron energy) instead of 27.5 ms (5.6 meV), the detailed shape in the background was carefully estimated by the method described in Appendix. The deduced frame overlap background and constant background for the TOF spectrum of the ^{157}Gd 20-μm^t sample before and after the background subtraction are shown in Figure 17. In this step, the uncertainties of this background subtraction were deduced from the uncertainties of the fitted parameters.

Relative neutron intensities per proton beam shot were derived from the results of the Al foil measurements with the Ge detectors as described in Section 3.2.6. After subtracting the frame overlap and constant backgrounds, each TOF spectrum was renormalized to 7.2×10^2 counts with the Ge detectors. The result of 7.2×10^2 counts is equivalent to the proton beam power of 1 kWh at the measurement of the ^{157}Gd 20-μm^t sample. Uncertainties due to the neutron intensity normalization were deduced from the statistical uncertainties with the Ge detectors.

The sample-independent background for the item (3) was derived from the measured TOF spectrum of the Blank sample with the dead time correction and the subtraction of the frame overlap and constant backgrounds. The backgrounds due to the Al foils in the ^{155}Gd and ^{157}Gd samples for the item (4) were deduced from the spectrum of the Al foil sample. The number of neutrons injected to the Al foils was attenuated due to self-shielding effects of ^{155}Gd and ^{157}Gd since the capture cross sections of ^{155}Gd and ^{157}Gd are very large. Therefore, the influence of the effects on the background due to the Al foils should be considered. The self-shielding effects for the Al foils in the Gd samples were deduced by using the Monte-Carlo simulation code, PHITS [35]. The cross-section data used in the simulation were taken from JENDL-4.0. To derive the uncertainties, correction factors for ideal samples with area densities larger by the 1-σ uncertainty than those in the actual samples were calculated. The differences between the correction factors for the actual samples and those for the ideal samples were considered as uncertainties due to the correction. The deduced net TOF spectra for the ^{155}Gd and ^{157}Gd samples are shown in Figure 18.

4.3.4. Correction for multiple scattering effects

The multiple scattering correction in the ^{155}Gd and ^{157}Gd samples was also made using the PHITS. The calculated multiple scattering correction factors for the ^{155}Gd and ^{157}Gd samples are shown in Figure 19 in which the multiple scattering correction factors are smaller than 1.0034 in the neutron energy range below 1 eV (TOF region over 2 ms). To derive the

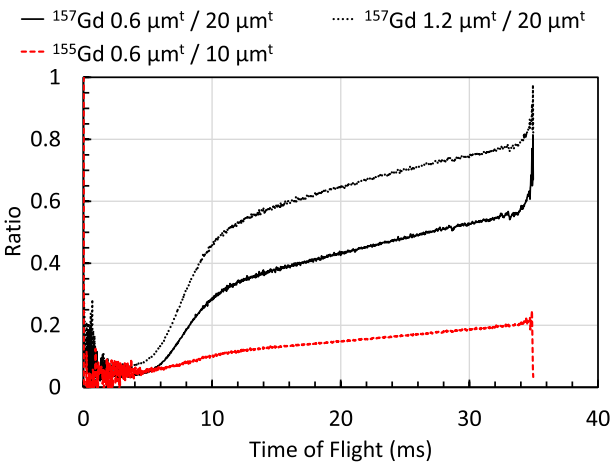

Figure 20. Ratio of the detected capture event rate for the ^{155}Gd 0.6-μm^t sample to that for the ^{155}Gd 10-μm^t sample and ratios of the detected capture event rates for the ^{157}Gd 0.6-μm^t and ^{157}Gd 1.2-μm^t samples to that for the ^{157}Gd 20-μm^t sample.

uncertainties, differences between the correction factors for the actual samples and those for the ideal samples with area densities larger than the 1-σ uncertainty comparison to those in the actual samples were considered, as well as the case of the self-shielding effects described in Section 4.3.3.

The ratios of the detected capture event rates for the ^{157}Gd 0.6-μm^t and ^{157}Gd 1.2-μm^t samples to that for the ^{157}Gd 20-μm^t sample and the ratio of the detected capture event rate for the ^{155}Gd 0.6-μm^t sample to that for the ^{155}Gd 10-μm^t sample were calculated using the net TOF spectrum and the multiple scattering correction factors. The obtained ratios with the multiple scattering corrections are shown in Figure 20. By using the ratios, the neutron spectrum was canceled out and smoothed shapes were obtained.

4.4. Results

The capture cross sections for ^{157}Gd deduced from Equation (14) and the ratios in Figure 20 are shown in Figure 21 together with that of JENDL-4.0.

The capture cross section of the ^{155}Gd sample was also deduced from Equation (15) and the ratio of the capture event rates, after subtracting the contribution of ^{157}Gd. In the subtraction, the result of the '^{157}Gd 1.2-μm^t sample / ^{157}Gd 20-μm^t sample' analysis was used as the capture cross section of ^{157}Gd. The derived capture cross section of ^{155}Gd is shown in Figure 22.

In this analysis, the statistical uncertainty and uncertainties due to the dead time correction, the frame overlap subtraction, neutron intensity normalization, background from the Al foils, multiple scattering correction, averaged sample mass, isotopic composition, sample setting accuracy, thickness non-uniformity and subtraction of ^{157}Gd contribution were considered. The

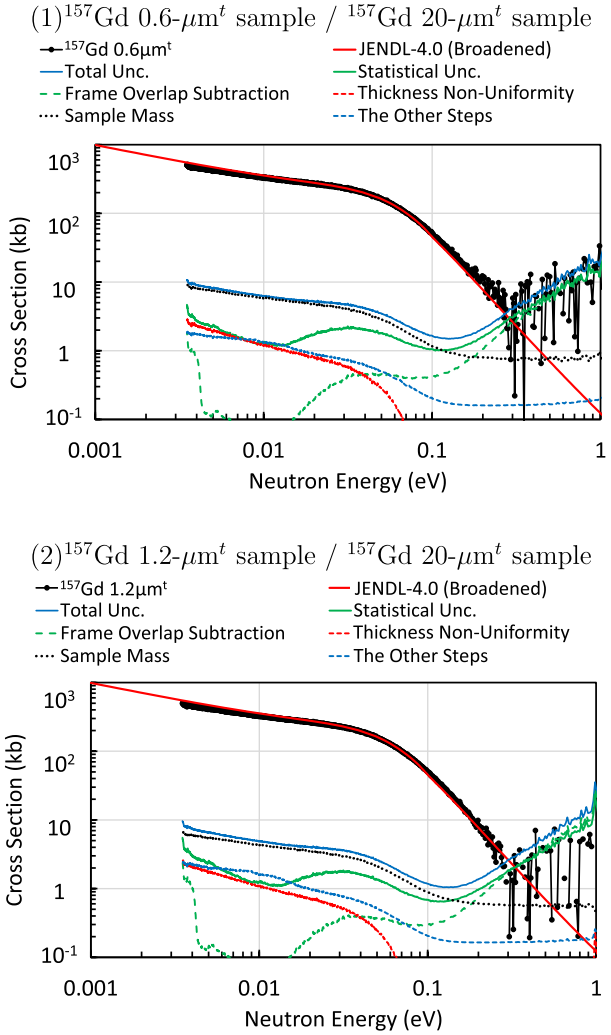

Figure 21. Determined capture cross sections of ^{157}Gd and some of uncertainties (total and statistical uncertainties, uncertainties due to frame overlap subtraction, thickness non-uniformity of the samples and sample mass) together with JENDL-4.0 at the temperature of 300 K (broadened with the resolution function of ANNRI). The other relevant uncertainties, not shown explicitly, are those due to dead time correction, neutron intensity normalization, background from the Al foils, isotopic ratio, multiple scattering correction, and sample setting.

uncertainty due to the dead time correction, the frame overlap subtraction, the neutron intensity normalization, the background from the Al foils and the multiple scattering correction are described in Section 4.3. The uncertainty due to the sample mass was derived from the uncertainties of the area density, as described in Table 6. The uncertainty due to the isotopic composition affects the area density. In the total cross-section measurements described in Section 3, these uncertainties are included in the uncertainties related to the sample mass. In Equations (14) and (15), the uncertainties of the sample area densities affect $N_{155\ or\ 157\ thin}$ and $N_{155\ or\ 157\ thick}$ independently, but the isotopic composition affected both at the same time. Therefore, the uncertainty due to isotopic composition was separated from the uncertainty related to sample mass. The sample

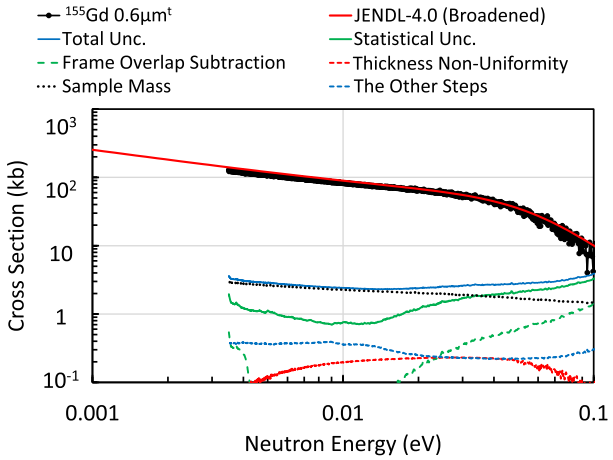

Figure 22. Determined capture cross section of ^{155}Gd, and some of uncertainties (total and statistical uncertainties, uncertainties due to frame overlap subtraction, thickness non-uniformity of the samples and sample mass) together with JENDL-4.0 at the temperature of 300 K (broadened with the resolution function of ANNRI). The other relevant uncertainties, not shown explicitly, are those due to dead time correction, neutron intensity normalization, background from the Al foils, isotopic ratio, multiple scattering correction, sample setting, and subtraction of ^{157}Gd contribution.

setting accuracy was estimated smaller than 5 degrees with respect to the vertical direction to the neutron beam. The uncertainty due to thickness non-uniformity was estimated from the difference between the results with the truncated normal distribution calculated from Equations (14) and (15) and without considering thickness dispersion calculated from Equations (10) and (11). The uncertainty due to the subtraction of ^{157}Gd contribution was derived from the uncertainties of the isotopic ratio and the uncertainty of the deduced capture cross section of ^{157}Gd . Some of the derived uncertainties are also shown in Figures 21 and 22.

The numerical values of these uncertainties at the thermal energy were summarized in Table 7. The primary uncertainty component comes from the statistical uncertainty and the uncertainty due to sample mass. This situation is identical to the total cross-section measurements, as listed in Table 5.

5. Discussion

Figures 23 and 24 depict the obtained total and capture cross sections for ^{155}Gd and ^{157}Gd in comparison with the total cross sections in JENDL-4.0.

In the neutron energy range below 0.2 eV, the total cross sections of ^{155}Gd and ^{157}Gd are almost equal to the capture cross sections, since the capture cross sections are much larger than their elastic scattering cross sections. The obtained cross sections with both methods are consistent, as shown in Figures 23 and 24. This fact increases the reliability of the present cross section for both ^{155}Gd and ^{157}Gd. In the neutron energy range above 0.02 eV, the obtained results of ^{155}Gd and ^{157}Gd agree with the values in JENDL-4.0. However, in the neutron energy range below 0.02 eV, the difference between the present results and the evaluated capture cross section of JENDL-4.0 becomes large as the neutron energy decreases.

The obtained thermal cross sections of ^{155}Gd and ^{157}Gd are listed in Table 1 in comparison with the experimental results in the literature and the evaluated values. The present results for ^{155}Gd (i.e. 59.4 $\pm$ 1.7 kb for total cross section and 59.0 $\pm$ 2.5 kb for capture cross section) are slightly smaller than the values of the evaluated libraries and literature, but consistent within their uncertainties. For the cross sections of ^{157}Gd, the present results (i.e. 251.9 $\pm$ 4.6 kb for the total cross section and 250.2 $\pm$ 5.0 and 247.4 $\pm$ 3.9 kb for the capture cross section) are slightly smaller but consistent with ENDF/B-VIII.0 (253.9 kb) and JENDL-4.0 (254.1 kb). The results agree with the experimental data by Møller et al. (254 $\pm$ 2 kb) and Mastromarco et al. (239.8 $\pm$ 8.4 kb), but disagree with the data by Leinweber et al. (226 kb).

6. Summary

The neutron total and capture cross sections of ^{155}Gd and ^{157}Gd were measured in the J-PARC · MLF · ANNRI.

The neutron total cross sections were determined by the well-established neutron transmission method

Table 7. Details of uncertainties for the estimated capture cross sections of ^{155}Gd and ^{157}Gd at the thermal energy.

	^{155}Gd (kb)	^{157}Gd (kb)	
	^{155}Gd 0.6-μm^t sample	^{157}Gd 0.6-μm^t sample	^{157}Gd 1.2-μm^t sample
Estimated cross section	59.0 $\pm$ 2.5	250.2 $\pm$ 5.0	247.4 $\pm$ 3.9
Statistical uncertainty	1.5	2.0	1.8
Dead time correction	0.1	0.2	0.3
Frame overlap subtraction	0.3	0.3	0.3
Neutron intensity normalization	0.2	0.5	0.6
Background from Al foils	$<$ 0.1	$<$ 0.1	$<$ 0.1
Multiple scattering correction	$<$ 0.1	$<$ 0.1	$<$ 0.1
Sample mass	2.0	4.4	3.3
Isotopic composition	$<$ 0.1	$<$ 0.1	$<$ 0.1
Sample setting accuracy	0.2	0.6	0.6
Thickness non-uniformity	0.1	0.7	0.6
^{157}Gd contribution	$<$ 0.1	–	–

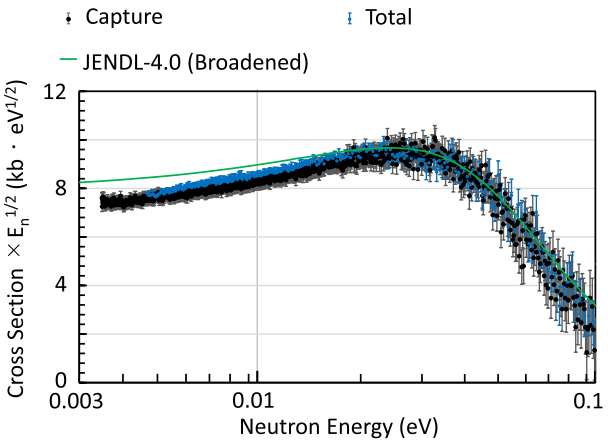

Figure 23. Deduced total and capture cross sections (multiplied by $E_n^{1/2}$) of ^{155}Gd together with the total cross sections in JENDL-4.0 at the temperature of 300 K (broadened with the resolution function of ANNRI). The error bars represent the total uncertainties.

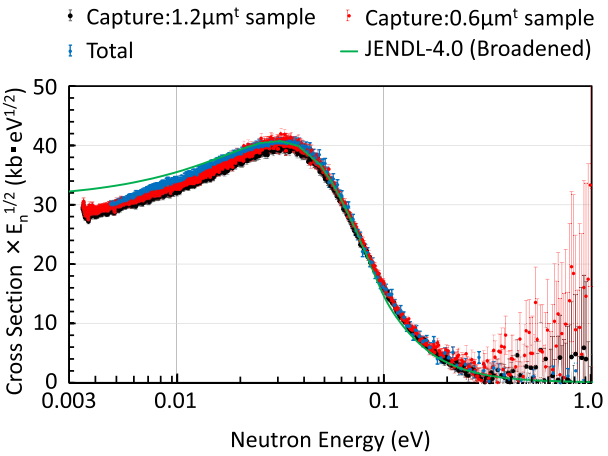

Figure 24. Obtained total and capture cross sections (multiplied by $E_n^{1/2}$) of ^{157}Gd together with the total cross sections in JENDL-4.0 at the temperature of 300 K (broadened with the resolution function of ANNRI). The error bars represent the total uncertainties.

with the enriched ^{6}Li- and ^{7}Li-glass detectors in the energy region from 5 to 100 meV. At the thermal energy, the neutron total cross-section result in 59.4 ± 1.7 and 251.9 ± 4.6 kb for ^{155}Gd and ^{157}Gd, respectively.

The neutron capture cross sections were determined with the innovative method by taking the ratio of the detected capture event rate between the thin and thick samples. By applying this method, the neutron spectrum and detection efficiency of the spectrometer were canceled out and the absolute capture cross sections were determined in the energy region from 3.5 to 100 meV. At the thermal energy, the capture cross sections were measured to be 59.0 ± 2.5 kb for ^{155}Gd and 250.2 ± 5.0 and 247.4 ± 3.9 kb for ^{157}Gd.

The obtained thermal cross sections of ^{155}Gd are slightly smaller but consistent with the values in JENDL-4.0. The results are also in agreement with the experimental values given by Mastromarco et al. and Leinweber et al. The obtained thermal cross sections of ^{157}Gd are consistent with the values in JENDL-4.0. The present thermal capture cross sections agree with the data by Mastromarco et al. within 1.4 standard deviations but have a difference in comparison with the experimental result by Leinweber et al.

The present total and capture cross sections based on different measurements agree well with each other, for both ^{155}Gd and ^{157}Gd. This fact makes the reliability of the present results enhanced.

Acknowledgments

The neutron experiments at the MLF of the J-PARC were performed under the user programs (Proposal No. 2016P1000, 2018P1000, and 2012B0093). The present study includes the result of "Research and Development for accuracy improvement of neutron nuclear data on minor actinides" entrusted to the Japan Atomic Energy Agency by the Ministry of Education, Culture, Sports, Science and Technology of Japan (MEXT).

Disclosure statement

No potential conflict of interest was reported by the author(s).

ORCID

Gerard Rovira http://orcid.org/0000-0002-3031-6204
Hideo Harada http://orcid.org/0000-0002-9797-0745

References

[1] Masterson RE. Introduction to nuclear reactor physics. Boca Raton: CRC Press; 2017. https://www.taylorfrancis.com/books/mono/10.1201/9781315118055/introduction-nuclear-reactor-physics-robert-masterson
[2] Goldstein L, Strasser AA. A comparison of gadolinia and boron for burnable poison applications in pressurized water reactors. Nucl Technol. 1983;60(3):352–361. Available from.
[3] Tattersall R, Rose H, Pattenden S, et al. Pile oscillator measurements of resonance absorption integrals. J Nucl Sci. 1960;12(1):32–46. http://www.sciencedirect.com/science/article/pii/0368326560900062
[4] Bjerrum Møller H, Shore F, Sailor V. Low-energy neutron resonances in erbium and gadolinium. Nucl Sci Eng. 1960;8(3):183–192. Available from.
[5] Ohno Y, Asami T, Okamoto K, et al. The Total Cross Sections of Some Rare-Earth Elements for 2200 m/sec Neutrons. JAERI memo 3305 EANDC(J)-10. Tokaimura: Japan Atomic Energy Research Institute. 1968.
[6] Sun G, Byun S, Choi H. Prompt k_0-factors and relative gamma-emission intensities for the strong non-1/v absorbers ^{113}Cd, ^{149}Sm, ^{151}Eu and ^{155,157}Gd. J Radioanal Nucl Chem.2003;256(3):541–552.

[7] Leinweber G, Barry DP, Trbovich MJ, et al. Neutron capture and total cross-section measurements and resonance parameters of gadolinium. Nucl Sci Eng. 2006;154(3):261–279. Available from.
[8] Noguere G, Archier P, Gruel A, et al. Interpretation of pile-oscillation measurements by the integral data assimilation technique. Nucl. Instrum 2011;629 (1):288–295. https://www.sciencedirect.com/science/article/pii/S0168900210024964
[9] Choi H, Firestone R, Basunia M, et al. Radiative capture cross sections of ^{155,157}Gd for thermal neutrons. Nucl Sci Eng. 2014;177(2):219–232. Available from.
[10] Mastromarco M, Manna A, Aberle O, et al. Cross section measurements of ^{155,157}Gd (n,γ) induced by thermal and epithermal neutrons. Eur Phys J A. 2019;55(1):9.
[11] Shibata K, Iwamoto O, Nakagawa T, et al. JENDL-4.0: a new library for nuclear science and engineering. J Nucl Sci Technol. 2011;48(1):1–30. Available from.
[12] Brown D, Chadwick M, Capote R, et al. ENDF/B-VIII.0: the 8th major release of the nuclear reaction data library with CIELO-project cross sections, new standards and thermal scattering data. Nucl Data Sheets. Special Issue on Nuclear Reaction Data; Available from. 2018;148:1–142.
[13] Mughabghab S. Atlas of neutron resonances. 6th ed. Amsterdan: Elsevier Science; 2018.
[14] Shibata K, Kawano T, Nakagawa T, et al. Japanese evaluated nuclear data library version 3 revision- 3: jendl-3.3. J Nucl Sci Technol. 2002;39(11):1125–1136.
[15] Perret G, Murphy MF, Jatuff F, et al. Impact of new gadolinium cross sections on reaction rate distributions in 10×10 BWR assemblies. Nucl Sci Eng. 2009;163(1):17–25.
[16] Chiba G, Okumura K, Sugino K, et al. Jendl-4.0 benchmarking for fission reactor applications. J Nucl Sci Technol. 2011;48(2):172–187. Available from https://www.tandfonline.com/doi/abs/10.1080/18811248.2011.9711692
[17] Rocchi F, Guglielmelli A, Castelluccio DM, et al. Reassessment of gadolinium odd isotopes neutron cross sections: scientific motivations and sensitivity-uncertainty analysis on lwr fuel assembly criticality calculations. EPJ Nucl Sci Technol. 2017;3:21.
[18] Maekawa F, Harada M, Oikawa K, et al. First neutron production utilizing J-PARC pulsed spallation neutron source JSNS and neutronic performance demonstrated. Nucl Instrum Methods Phys Res A. 2010;620(2):159–165. Available from http://www.sciencedirect.com/science/article/pii/S0168900210008223
[19] Terada K, Kimura A, Nakao T, et al. Measurements of neutron total and capture cross sections of ^{241}Am with ANNRI at J-PARC. J Nucl Sci Technol. 2018;55 (10):1198–1211. Available from.
[20] Igashira M, Kiyanagi Y, Oshima M. Nuclear data study at J-PARC BL04. Nucl Instrum Methods Phys Res A. 2009;600(1):332–334.
[21] Kino K, Furusaka M, Hiraga F, et al. Measurement of energy spectra and spatial distributions of neutron beams provided by the ANNRI beamline for capture cross-section measurements at the J-PARC/MLF. Nucl Instrum Methods Phys Res A. 2011;626-627:58–66. Available from http://www.sciencedirect.com/science/article/pii/S0168900210023387
[22] Shibahara Y, Hori J, Takamiya K, et al. High precision analysis of isotopic composition for samples used for nuclear cross-section measurements. EPJ Web Conf. 2017;146:03028.
[23] Kimura A, Nakamura S, Terada K, et al. Measurements of the ^{243}Am neutron capture and total cross sections with ANNRI at J-PARC. J Nucl Sci Technol. 2019;56(6):479–492.
[24] Nakao T, Terada K, Kimura A, et al. Developments of a new data acquisition system at ANNRI. In: ND 2016: International Conference on Nuclear Data for Science and Technology Bruges; Vol. 146; EDP Sciences (EPJ Web of Conferences); 2017. p. 03021. https://www.epj-conferences.org/articles/epjconf/abs/2017/15/epjconf-nd2016_03021/epjconf-nd2016_03021.html
[25] CAEN SpA. Digital pulse processing for charge integration, caen user manual um2089. Viareggio, Italy 2015.
[26] Kin T, Furutaka K, Goko S, et al. The" 4π Ge spectrometer" for measurements of neutron capture cross sections by the TOF method at the J-PARC/MLF/ANNRI. J Korean Phys Soc. 2011;59(23):1769–1772.
[27] Yousaf M, Akyurek T, Usman S. A comparison of traditional and hybrid radiation detector dead- time models and detector behavior. Prog Nucl Energy. 2015;83:177–185. Available from: https://www.sciencedirect.com/science/article/pii/S0149197015000839
[28] Kimura A, Fujii T, Fukutani S, et al. Neutron-capture cross-sections of ^{244}Cm and ^{246}Cm measured with an array of large germanium detectors in the ANNRI at J- PARC/MLF. J Nucl Sci Technol. 2012;49 (7):708–724. Available from.
[29] Kino K, Furusaka M, Hiraga F, et al. Energy resolution of pulsed neutron beam provided by the ANNRI beamline at the J-PARC/MLF. Nucl Instrum Methods Phys Res A. 2014;736:66–74. Available from http://www.sciencedirect.com/science/article/pii/S0168900213013028
[30] Rovira G, Katabuchi T, Tosaka K, et al. Neutron capture cross-section measurement and resolved resonance analysis of 237Np. J Nucl Sci Technol. 2020;57(1):24–39.
[31] Hirose K, Furutaka K, Hara KY, et al. Cross-section measurement of ^{237}Np(n,γ) from 10 meV to 1 keV at Japan proton accelerator research complex. J Nucl Sci Technol. 2013;50(2):188–200. Available from.
[32] Katabuchi T, Igashira M, Matsuhashi T, et al. Nuclear data measurement using the accurate neutron-nucleus reaction measurement instrument (ANNRI) in the Japan Proton accelerator research complex (J-PARC). Vienna: IAEA; 2014. IAEA-TECDOC 1743.
[33] Katabuchi T, Matsuhashi T, Terada K, et al. Pulse-width analysis for neutron capture cross-section measurement using an NaI(Tl) detector. Nucl Instrum Methods Phys Res A. 2014;764:369–377. Available from http://www.sciencedirect.com/science/article/pii/S0168900214009206
[34] Macklin RL, Gibbons JH. Capture-cross-section studies for 30-220-kev neutrons using a new technique. Phys Rev. 1967 Jul;159:1007–1012. Available from https://link.aps.org/doi/10.1103/PhysRev.159.1007
[35] Sato T, Iwamoto Y, Hashimoto S, et al. Features of particle and heavy ion transport code system (PHITS) version 3.02. J Nucl Sci Technol. 2018;55(6):684–690

Appendix Influence of the disk chopper on the frame overlap background

The influence of the disk chopper was estimated in the analysis with the NaI(Tl) spectrometer. As reported in section 3.2.4, the frame overlap background and constant background were deduced with the wide range TOF spectrum every 58 shots. Figure 25 shows the wide range TOF spectrum of the ^{157}Gd 20-μm^t sample measurement in the TOF range of 40 to 80 ms .

As shown in Figure 25, the disk chopper was closed at 68.3 ms for the previous ($t_0 \approx -40$ ms) pulsed neutrons and opened at 71.3 ms for the present ($t_0 \approx 0$ ms) pulsed neutrons. The tail part of the previous pulsed neutrons ($t_0 \approx -40$ ms) was observed in TOF range before 66 ms and that of the present ($t_0 = 0$ ms) pulsed neutrons was observed after 72 ms.

A fitting function $F_{F+C}(t)$ is described as follows:

$$F_{F+C}(t) = (F(t+40\ \text{ms}) - \beta) \times R_{ave}(t+40\ \text{ms}) + (F(t) - \beta) \times R_{ave}(t) + \beta, \quad \text{(A.1)}$$

$$F(t) = \alpha \times \exp(-\frac{t}{t_c}) + \beta, \quad \text{(A.2)}$$

where $R_{ave}(t)$ is the transmission ratio of the disk chopper, t is the TOF in ms at the sample position and α, β and t_c are fitting parameters.

In the disk chopper, a semicircular shape plate made of boron carbide rotates at 25 Hz. Figure 26 shows a simple diagram of the relationship between the neutron beam and the disk chopper. In Figure 26, the circle in light gray means the neutron beam: C_n is a center of the neutron beam: the dark gray part means the boron-carbide plate of the disk chopper: C_d is the center of the plate: L_{dn} is the distance between the centers of the disk chopper and the neutron beam, and r_n is the radius of the neutron beam.

The relationship between the angle θ in Figure 26 and the TOF at the sample position is described as follows with considering the flight time from the disk chopper to the sample.

$$\theta = 2\pi \times \frac{t}{40} \times \frac{L_D}{L_S} + \theta_0, \quad \text{(A.3)}$$

where L_D is the flight length at the disk chopper (installed at 15.08 m), L_S is the flight length at the sample position

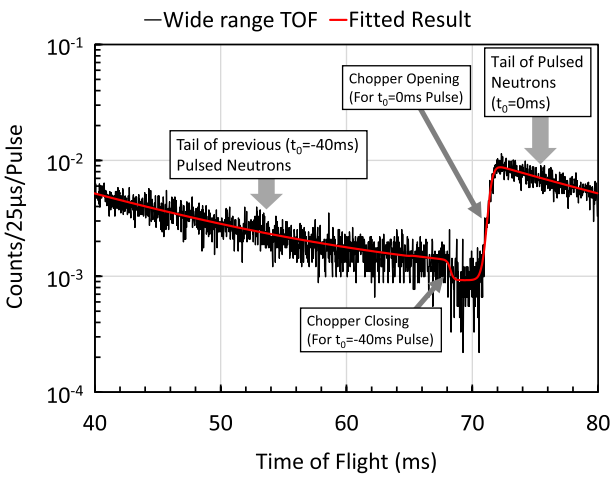

Figure 25. Wide range TOF spectrum with the ^{157}Gd 20-μm^t sample and fitted result in TOF range after 40 ms.

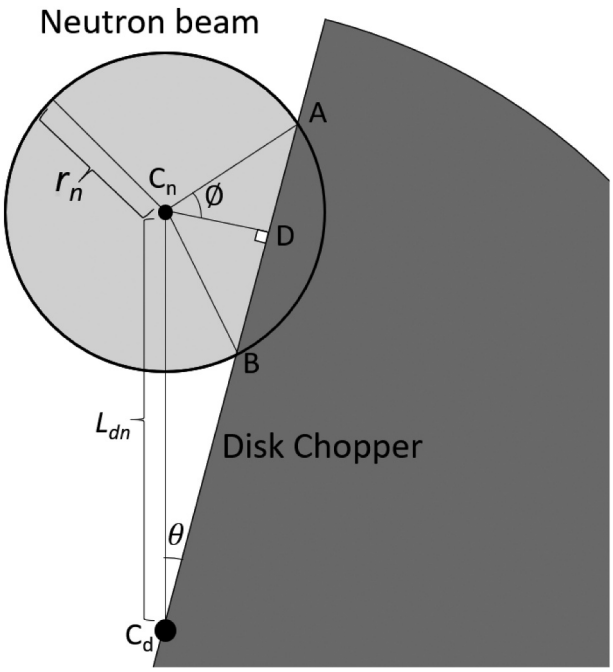

Figure 26. Diagram of the neutron beam (circle in light gray) and the boron-carbide plate of the disk chopper (semicircle in dark gray).

(27.9 m) and θ_0 is the angle at $t = 0$. A relationship between the angle θ and ϕ in Figure 26 is derived as follows:

$$distance\ C_nD = L_{dn} \times \sin\theta = r_n \times \cos\phi,$$

$$\phi = \arccos\left(\sin\theta \frac{L_{dn}}{r_n}\right). \quad \text{(A.4)}$$

Using θ and ϕ, the transmission ratio of the disk chopper, $R(\theta)$, in the setup of Figure 26 is described by the following equations:

$$R(\theta) = \begin{cases} 0 & (L_{dn} \times \sin\theta < -r_n), \\ ((\pi - \phi) \times r_n^2 + \sin\phi \times \sin\theta \times L_{dn} \times r_n)/(\pi \times r_n^2) & (-r_n < L_{dn} \times \sin(\theta) < r_n), \\ 1 & (r_n < L_{dn} \times \sin(\theta)). \end{cases} \quad \text{(A.5)}$$

Since the disk chopper is mechanically controlled, θ_0 has a fluctuation. By assuming a truncated normal distribution for θ_0, the averaged transmission ratio, $R_{ave}(t)$, is expressed as the following equation:

$$R_{ave}(t) = \int_a^b f(x;\mu,\sigma,a,b) \times R(\theta + x)dx, \quad \text{(A.6)}$$

where $\mu = 0$, $\sigma = \sigma_{\Delta\theta}$, $a = -\pi/16$, $b = \pi/16$, $\sigma_{\Delta\theta}$ is the standard deviation of fluctuation of θ_0.

In the experiments, the first 58 of 62 proton shots were provided to the MLF and the last four shots were supplied to the other facilities. At the first pulsed neutrons of the continuous 58 pulsed neutrons, the overlapping neutrons were negligible and only the constant part (the third term, β, in Equation (A.1)) existed because the preceding proton shots were not delivered to MLF. At the second pulsed neutrons of the 58 pulsed neutrons, the first term in Equation (A.1) did not exist, because the proton shots before the last two were not delivered to MLF. Thus, the frame overlap background and constant background were deduced by the following equation:

$$B_{F+C}(t) = \frac{56}{58} \times (F(t + 80\ \mathrm{ms}) - \beta) \times R_{ave}(t + 80\ \mathrm{ms}) + \frac{57}{58} \times (F(t + 40\ \mathrm{ms}) - \beta) \times R_{ave}(t + 40\ \mathrm{ms}) + \beta \tag{A.7}$$

It was very challenging to fix the all parameters simultaneously. Therefore, in the present analysis, the exponential part, 40 ms $< t <$ 66 ms, of the wide range TOF spectrum was fitted by the equation $F(t -$ 40 ms $)$, thus the parameters α, β and t_c were obtained. Next, in the opening part of the disk chopper, 70 ms $< t <$ 74 ms, the spectrum was fitted by the equation $(F(t) - \beta) \times R_{ave}(t) + \beta$ and the parameters of θ_0, $\sigma_{\Delta\theta}$, L_{dn}/r_n were derived. Deduced $F_{F+C}(t)$ is shown in Figure 25. The fitted result was in good agreement with the wide range TOF spectrum.